# Facet-Dependent Electron Trapping in TiO$_2$ Nanocrystals

Suzanne K. Wallace and Keith P. Mckenna*

Department of Physics, University of York, Heslington, York YO10 5DD, United Kingdom

S *Supporting Information*

ABSTRACT: The trapping of electrons at surfaces of nanocrystalline titanium dioxide can be decisive in controlling performance for diverse applications in photocatalysis, energy storage, and solar energy generation. Here, we employ first-principles calculations to elucidate the factors which influence electron trapping for all low index surfaces of rutile TiO$_2$. We show that different surface orientations exhibit markedly different electron affinities: some preferring to trap electrons with others repelling electrons. We demonstrate that local variations in trapping energy are linked to variations in electrostatic potential and ion coordination providing atomistic insight into this effect. The equilibrium nanocrystal morphology exposes both electron-trapping and electron-repelling facets and therefore is predicted to possess highly anisotropic electron-trapping properties. We discuss how knowledge of surface-specific trapping properties can be utilized to design a number of nanocrystal morphologies which may offer improved performance for applications.
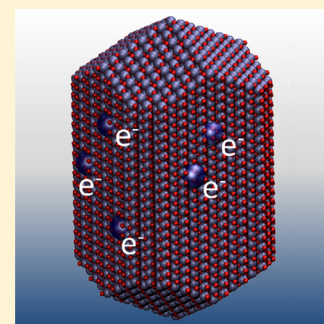
INTRODUCTION

Electron trapping in nanocrystalline titanium dioxide (TiO$_2$) is an issue of fundamental and technological significance under-pinning applications in areas such as solar energy generation, photocatalysis, and portable energy storage.[1−6] Both first-principles calculations[7−10] and electron paramagnetic resonance (EPR) studies[11−14] provide clear evidence that electrons form small polarons in the bulk rutile TiO$_2$ crystal. The trapping of electrons, which may be generated by photo-excitation or electron injection, leads to a reduction of Ti cations from the Ti^{4+} to the Ti^{3+} valence state. Critical for applications in photocatalysis, electrons also trap at the surface of nanocrystals, but probing the nature of these surface traps experimentally (e.g., using EPR or scanning probe microscopy) has proved extremely challenging.[10−15] On the other hand, there have been relatively few theoretical studies of the trapping of electrons at rutile TiO$_2$ surfaces. The only rutile TiO$_2$ surface to have been studied in such a way is the (110) surface where electrons were found to be preferentially trapped in the subsurface layer.[16,17] While the (110) surface is predicted to be the most stable in rutile TiO$_2$,[18] other surface facets present in real synthesized nanocrystals may exhibit quite different electron-trapping properties.

A deeper understanding of the interaction of electrons with TiO$_2$ nanocrystal surfaces is needed urgently as it can be decisive in controlling performance for numerous applications. For example, the trapping of photogenerated charge at nanocrystal surfaces can facilitate oxidation or reduction reactions. This is the principle of operation of TiO$_2$ photocatalysts which find applications in water splitting,[3] water purification,[19] and self-cleaning glass.[5] Therefore, optimal nanocrystals for photocatalysis should expose surfaces which can sustain a high concentration of active Ti^{3+} surface sites. A different example is the trapping of photoinjected electrons in the photoanode of TiO$_2$ dye-sensitized solar cells (DSSCs).[20]

In this case electron trapping at surfaces is undesirable as it hinders the flow of electrons through the nanoporous network and increases the rate of electron−hole recombination, both of which reduce device efficiency. Optimal nanocrystals for DSSC photoanodes would expose surfaces which have low affinity toward electrons while at the same time allowing for efficient injection of electrons from the dye molecules and facile transfer of electrons between nanocrystal interfaces. These two examples underscore the need for a detailed understanding of the trapping of electrons in nanocrystals and the factors that influence it in order to form a rational basis for the optimization of nanomaterials for applications.

First-principles theoretical calculations, mainly within the framework of density functional theory (DFT), have proved invaluable in providing guidance and an atomistic under-standing of nanocrystalline TiO$_2$ and associated defects. However, DFT with standard local or semilocal approximations for exchange and correlation is inadequate for describing electron trapping and the properties of many defects in TiO$_2$ owing to the self-interaction error (SIE).[21−23] Hybrid-DFT approaches which include nonlocal exchange contributions[24] and DFT+U methods[21,25,26] correct (at least in part) the SIE allowing for more reliable predictions. Such methods have been employed to investigate electron trapping in TiO$_2$ including studies of polaron formation in the ideal crystal,[7−10,27] electron trapping at intrinsic defects such as oxygen vacancies,[28−33] as well as at impurities, grain boundaries, and surfaces.[32,34−36] However, studies of electron trapping at rutile surfaces have been limited to only the (110) surface where the effect of vacancies, hydroxyls, and impurities on electron trapping have been studied.[16,17,37]
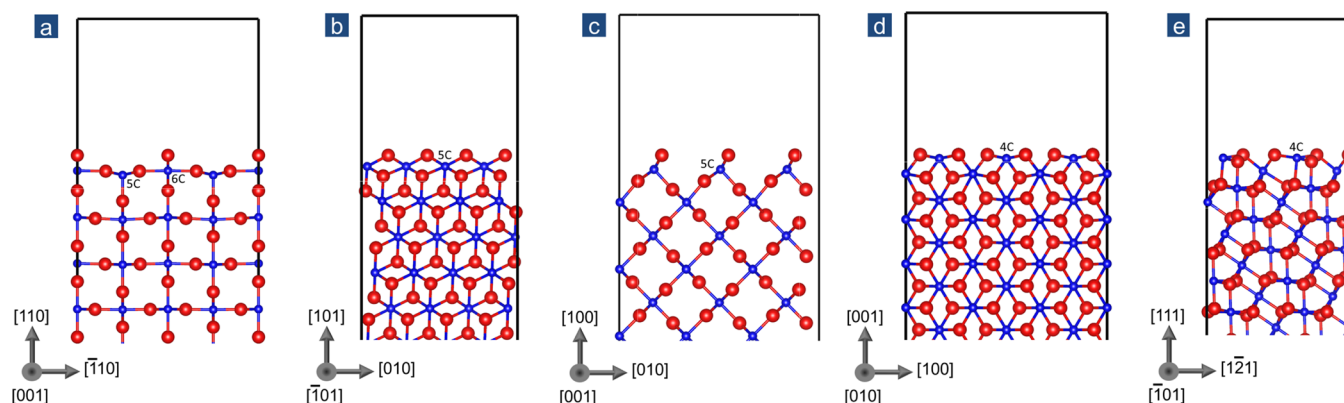
Figure 1. Optimized structures of the low-index surfaces of rutile TiO$_2$: (a) (110), (b) (101), (c) (100), (d) (001), and (e) (111). Large red and small blue spheres represent oxygen and titanium ions, respectively.

In this article, we shed light upon these issues by performing a detailed theoretical study of the trapping of electrons at all low index surfaces of rutile TiO$_2$. We show that electrons preferentially trap at the (001) and (110) surfaces but not at (111), (100), and (101) surfaces. Furthermore, we demonstrate that the markedly different electron-trapping properties of different surface orientations are connected to their distinct electrostatic and structural properties. On the basis of this atomistic insight we propose a number of nonequilibrium nanocrystal morphologies which may offer improved performance for photocatalyst and dye-sensitized solar cell applications.

■ THEORETICAL METHODS

Spin-polarized DFT calculations are performed using the projector-augmented wave (PAW) method as implemented within the Vienna ab initio simulation package.[38,39] We use the Perdew−Burke−Ernzerhof exchange correlation functional and correct for the SIE by employing a DFT+U approach.[26,40] Recent works have shown that hybrid-DFT functionals and DFT+U give a similar description of reduced bulk TiO$_2$.[28] Here, we employ a Hubbard-U parameter for the Ti 3d states with U_d = 4.2 eV which was shown previously to give good agreement to the spectroscopic properties of oxygen vacancies at the (110) surface.[41] Only the Ti 3d, Ti 4s, O 2s, and O 2p states are treated explicitly as valence electrons with all other electrons described within the PAW potential. Valence electron states are described within a plane wave basis set with a cutoff energy of 500 eV. Structural optimization is performed until forces on the ions are less than 0.01 eV/Å. Lattice parameters for the conventional unit cell of bulk rutile are obtained to within 2% of experiment (a = 4.67 Å and c = 3.03 Å) using a 5 × 5 × 5 Monkhorst−Pack k-point grid.

Surface slab models are constructed to model the structure and properties of the low index surfaces of rutile TiO$_2$. Three-dimensionally periodic slab models are constructed using the METADISE code[42] and incorporate a vacuum gap to separate the slab from its periodic images. The surface formation energy is calculated from the total energy of the surface slab, E_{surf}

$$\gamma = \frac{E_{surf} - nE_{bulk}}{2A} \tag{1}$$

where E_{bulk} is the total energy per formula unit of the bulk crystal; n is the number of formula units in the surface slab; and A is the area of the surface. The thickness of the slab and the size of the vacuum gap are increased until the formation energy

of each surface model converges to within 0.01 J·m^{-2}. Additionally, the total energies are converged with respect to the plane-wave cutoff energy and number of k-points in the Brillouin zone sampling. For the optimized surface slabs we compute on-site electrostatic potential energies for spherical unit test charges of radius 1.26 Å centered at each Ti ion by integrating over the self-consistently optimized electrostatic potential.

To characterize the interaction of electrons with each of the surfaces we attempt to localize electrons at all inequivalent cation sites within the slab and calculate the corresponding total energies. This approach was recently employed to investigate electron trapping at a TiO$_2$ grain boundary.[36] To reduce the effect of artificial interaction between the trapped electron and its periodic images the original surface slab models are expanded into supercells where the excess electron and its periodic image are separated by a minimum of 9 Å in each direction. Metastable configurations corresponding to an electron trapped at a given site were obtained in the following way. The initial charge density at the start of the self-consistent wave function optimization is chosen such that a single unpaired electron spin is localized at a given titanium site. We also create a precursor potential well for electron trapping by displacing neighboring oxygen ions around the titanium site away by 0.08 Å. This dilation of Ti−O bonds imitates the local distortion observed for the electron polaron in bulk rutile TiO$_2$.[16] The total energy of the system is then self-consistently optimized with respect to the position of all ions. This approach sometimes fails if the electron affinity is very low as the electron may instead transfer to a more favorable site during the self-consistent optimization. In some cases this can be resolved by temporarily increasing the value of the Hubbard-U parameter, e.g., to U_d = 7 eV, on the desired site in order to force trapping and obtain a better estimate for the geometry and charge density of the metastable state. This geometry and charge density are then used as an initial guess for a subsequent self-consistent geometry optimization using U_d = 4.2 eV on all Ti sites. Using these approaches only for a few very low electron affinity sites, we were unable to find any metastable trapped electron configuration.

■ RESULTS

Surface Properties and Equilibrium Nanocrystal Morphology. Given the symmetry of the rutile TiO$_2$ crystal there are five inequivalent low-index surface orientations:

{100}, {001}, {101}, {110}, and {111}. The optimized structure of each of these surfaces is shown in Figure 1 (see Methods section for details). We find that slabs of approximately 25 Å thickness and a vacuum gap of 10 Å are sufficient to obtain surface energies converged to 0.01 J·m^{-2} (see Supporting Information). Surface energies were calculated for both the Ti and O terminations of the {101}, {110}, and {111} surfaces, and only the most stable termination is presented (surface models terminating on oxygen ions had the lowest energies). Table 1 summarizes the calculated

**Table 1. Calculated Surface Formation Energies, γ, for the Low-Index Surfaces of Rutile TiO$_2$^{a}**

(hkl)	γ (J m^{-2})	Z	Δd (%)	f (%)
(100)	1.04	5	−1.9	13.1
(001)	1.68	4	−6.1	0.0
(101)	1.33	5	−1.6	34.5
(110)	0.86	5/6	−2.1/−0.1	52.4
(111)	1.80	4	−6.0	0.0

^{a}The coordination of Ti ions in the surface plane (Z), the average bond strain associated with these surface ions (Δd), and the contribution each surface makes to the total area of an equilibrium crystal (f) are given for each surface.

formation energies for each of the surfaces. Ramamoorthy et al. previously calculated the formation energy of the {100}, {001}, {101}, and {110} surfaces using the local density approximation, and their results are in very good agreement with our DFT+U calculated energies (within 0.08 J·m^{-2}).[18]

We now summarize some of the key structural features of the surfaces focusing specifically on the nature of Ti sites near the surface. The most stable surface, (110), has two inequivalent Ti sites in the surface plane. One of these sites is coordinated octahedrally to six neighboring oxygen ions (as in the bulk), while the other has its coordination reduced to five (denoted 6C and 5C in Figure 1). The overall high coordination of this surface helps explain its low formation energy. All Ti−O bonds involving the 5C site are shorter than for a Ti site in the bulk crystal (compressively strained by an average of 2%). The structural relaxation near the 6C surface site is more asymmetric with two bonds compressed by 5% and four bonds extended by about 3%. The remaining surfaces (Figure 1b−e) have only one inequivalent type of Ti ion in the surface plane. In the case of (100) and (101) these ions are both five coordinated, and again the bond distortion is asymmetric with both compressed and extended bonds. For the (111) and (001) surfaces, which have the highest formation energies, the coordination is reduced to four, and all of its Ti−O bonds are compressively strained by about 6%. One could naively consider the local structure around surface Ti sites as a guide to their ability to trap electrons. For example, electron trapping in the bulk crystal is associated with an average expansion of bonds to neighboring O ions by about 4% due to the reduced electrostatic attraction between Ti^{3+} and O^{2-}. Therefore, if one considered only the local structure one would predict that electron trapping would be most favorable in the cases where the compressive strain is smallest—i.e., the (101), (100), and (110) surfaces. In fact as we will show below this is not the case, and the local geometry alone does not provide a good guide as to whether a given Ti site will have a high electron affinity.

The surface energies calculated for the low index surfaces of rutile TiO$_2$ can be used to predict the equilibrium shape of nanocrystals using the Wulff construction.[18,43] Typical TiO$_2$ nanocrystal sizes in applications (e.g., for photoanodes in DSSCs) are of the order of tens of nanometers.[44−46] In this size range the Wulff construction should provide a reasonable prediction of the most stable nanocrystal shape as the contributions of edges and vertices to the surface energy can be neglected. Figure 2 shows the equilibrium nanocrystal shape
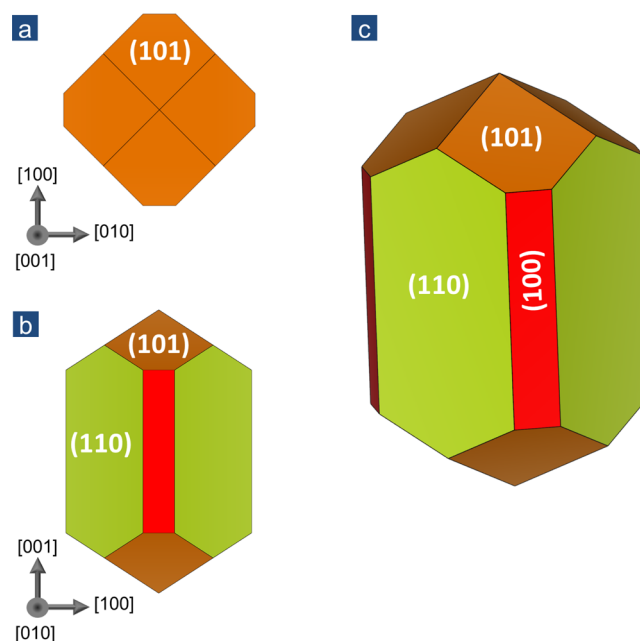
Figure 2. Predicted equilibrium shape of a rutile TiO$_2$ nanocrystal obtained using the DFT calculated surface energies and the Wulff construction. Figures a−c show different perspectives of the crystal morphology.

obtained using the DFT calculated surface energies. The dominant surface facet is of {110} type and constitutes over 50% of the exposed nanocrystal surface. {101} facets make the second biggest contribution to the nanocrystal surface (over 30%) with {100} facets accounting for the remainder.

Electron Trapping at the Rutile TiO$_2$(100) Surface. As an initial example we discuss results for electron trapping at the (100) surface before presenting all other surfaces in the following section. We focus on (100) first because we find it has electron-trapping properties which are markedly different from the previously studied (110) surface, and it is predicted to be present in equilibrium nanocrystals. As described in the Methods section we attempt to find metastable configurations corresponding to electrons trapped at all inequivalent Ti ions within the surface slab models (labeled 1−6 in Figure 3). Site 1 is in the center of the slab, and the optimized structure and spin density for a trapped electron at site 1 are shown in Figure 3a. Electron trapping is accompanied by outward displacement of neighboring oxygen ions. The bonds in the equatorial plane of the TiO$_6$ octahedra expand by 0.10 Å, while the axial bonds expand by 0.05 Å (corresponding to an average expansion of about 0.08 Å). The electron spin density is localized in a $|x^2 - y^2\rangle$ d-orbital (where x and y are in the equatorial plane of the TiO$_6$ octahedra) in excellent agreement with EPR results for the bulk rutile crystal.[13] We find the structure and spin density of an electron polaron trapped at site 1 is very similar to that
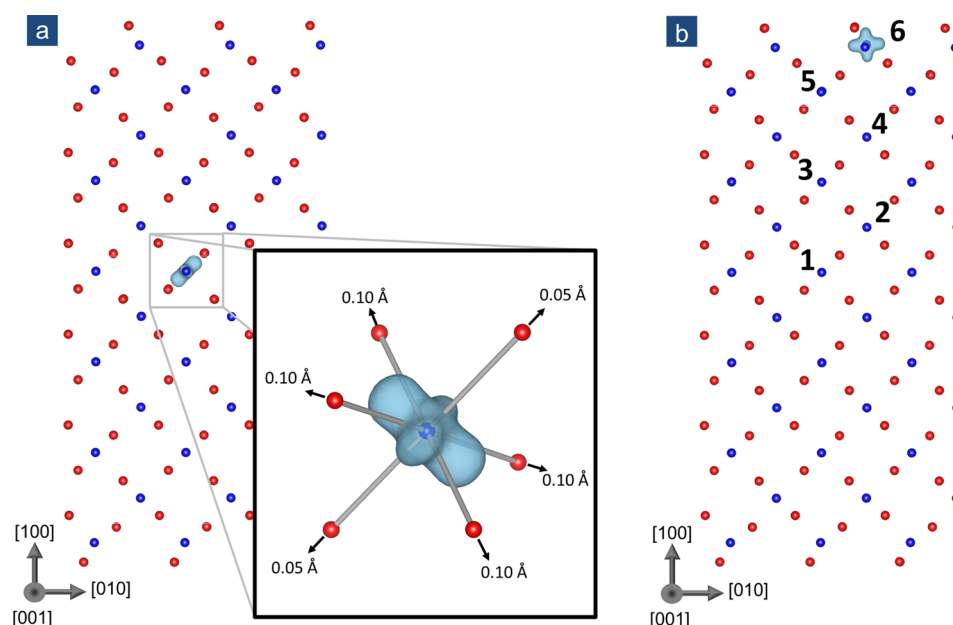
Figure 3. (a) Optimized structure of the (100) surface slab with an electron trapped in the center (site 1) with isosurfaces of electron spin density shown in light blue. The inset shows the oxygen octahedra surrounding the trapped electron with arrows indicating the local ionic distortion that accompanies electron trapping (note the orientation has been changed to more clearly show the local geometry and spin density). (b) The optimized structure of the same surface slab with an electron trapped near the surface. Inequivalent Ti sites in the slab are labeled 1−6. Red and blue spheres represent oxygen and titanium ions, respectively.

calculated in the bulk crystal indicating the site is deep enough inside the slab to be considered as a bulk polaron (see Supporting Information).

Metastable configurations corresponding to electrons trapped at sites 2−6 were obtained in a similar way. In order to compare the relative stability of electron polarons trapped at different sites we calculate

$$E_t = E_i - E_1$$

where E_i is the total energy of the polaron in site i defining a trapping energy with respect to an electron polaron in the bulk. Figure 4 shows how the trapping energy varies throughout the slab. It is notable that all of the trapping energies are positive (i.e., electrons trapped at sites 2−6 are less stable than the bulk-like site 1). The Ti site at the surface has the least favorable trapping energy of all sites in this surface slab ($E_t = 0.37$ eV) indicating that electron trapping at the (001) surface is extremely unfavorable. The local structure of this surface site provides no obvious clue as to why electron trapping is so unfavorable. However, we do see a correlation between the electron-trapping energy and the electrostatic potential at a given site. We calculate the on-site electrostatic potential energy of a negative charge located at each Ti site in the ideal (electron-free) surface slab u_i. To compare variations in the on-site electrostatic potential energy with respect to the bulk we calculate $U = u_i - u_1$ in a similar way as done for the trapping energy. The correlation between U and E_t shown in Figure 3 suggests that for this surface variations in trapping energy are mainly driven by electrostatic potential variations near the surface. This is consistent with trends observed for electron and hole trapping in a wide range of metal-oxide materials.[36,47−50]

Electron Trapping at Other Low Index Rutile TiO$_2$ Surfaces. In the same way as described above we attempted calculation of electron-trapping energies for all inequivalent Ti sites within each of the other surface slabs. Figure 5 summarizes
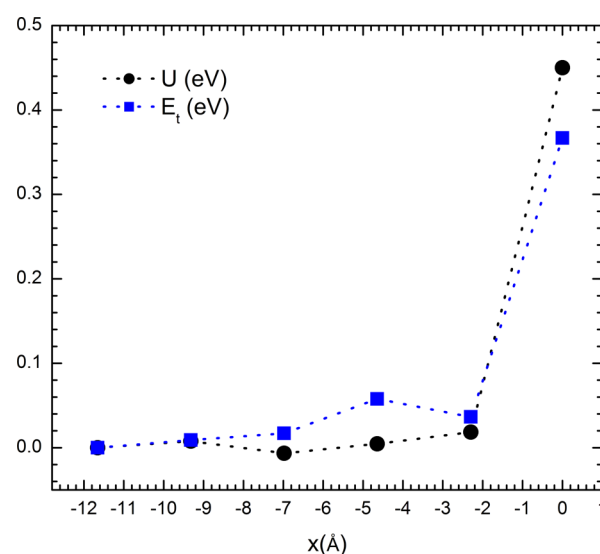
Figure 4. Variation of the electron-trapping energy (blue squares) and on-site electrostatic potential (black circles) with the position of the Ti ion in the surface slab ($x = 0$ Å corresponds to the position of the uppermost Ti ion in the surface slab, site 6 in Figure 3b).

the trapping energies and corresponding variations of on-site electrostatic potential energy. Of all the surfaces considered only the (110) and (001) surfaces present favorable sites for electron trapping with respect to the bulk. Site 9 in the (001) surface slab has the highest affinity toward electrons ($E_t = -0.40$ eV). Accompanying electron localization two bonds to neighboring oxygen ions positioned below site 9 in the slab extend by 0.14 Å, much greater than the distortion observed for a bulk polaron (0.08 Å). In the (110) surface slab electron trapping is most favorable at site 6 ($E_t = -0.28$ eV) which is a Ti ion in the subsurface layer in agreement with previous work.[16] Sites 2 and 8 are also favorable for electron trapping
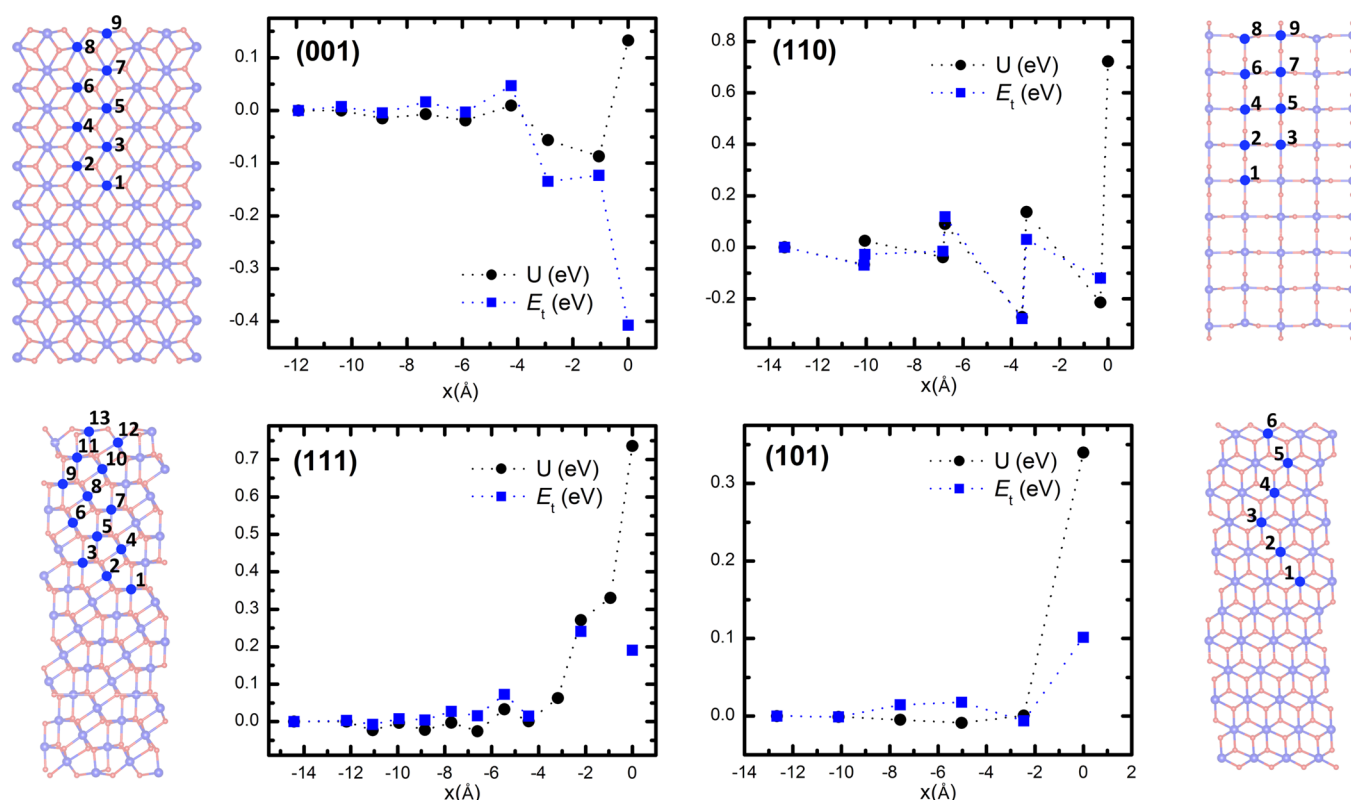
Figure 5. Variation of the electron-trapping energy (blue squares) and on-site electrostatic potential (black circles) with the position of the Ti ion in the (001), (110), (111), and (101) surface slabs ($x = 0$ Å corresponds to the position of the uppermost Ti ion in the surface slab). The structure of each surface slab is also shown with inequivalent Ti sites labeled. Small red and large blue spheres represent oxygen and titanium ions, respectively.

Table 2. Electron Trapping Energies (E_t) and On-Site Electrostatic Potentials Energies (U) for the Inequivalent Sites of All Low Index Surfaces of Rutile TiO$_2$[a]

| site	(110)		(101)		(100)		(001)		(111)	
	U	E_t	U	E_t	U	E_t	U	E_t	U	E_t
1	0.00	0.00	0.00	0.00	0.00	0.00	0.00	0.00	0.00	0.00
2	−0.07	−0.07	0.00	0.00	0.01	0.01	0.00	0.01	0.00	0.00
3	0.03	−0.03	0.00	0.01	−0.01	0.02	−0.02	0.00	−0.02	−0.01
4	−0.04	−0.02	−0.01	0.02	0.00	0.06	−0.01	0.02	0.00	0.01
5	0.09	0.12	0.00	−0.01	0.02	0.04	−0.02	0.00	−0.02	0.00
6	−0.27	−0.28	0.34	0.10	0.45	0.37	0.01	0.05	0.00	0.03
7	0.14	0.03					−0.06	−0.13	−0.02	0.02
8	−0.21	−0.12					−0.09	−0.12	0.03	0.07
9	0.72	−					0.13	−0.41	0.00	0.01
10									0.06	-
11									0.27	0.24
12									0.33	-
13									0.74	0.19

[a]All energies are measured in eV. Please refer to Figures 3 and 5 for definitions of the site numbers.

relative to the bulk. The (101), (100), and (111) surfaces were all found to repel electrons with the (100) surface being the most strongly repulsive. We were unable to find metastable trapped electron configurations at only three sites: site 9 in the (110) surface slab and sites 10 and 12 in the (111) surface slab. Attempts to localize the electron at these sites always resulted in the polaron transferring to a different site during the self-consistent optimization suggesting trapping at these sites is highly unfavorable. We discuss possible reasons for this below.

Table 2 summarizes the trapping energies and electrostatic potential energies of all sites within the surface slab models. As

seen for the (100) surface there is in general a very good correlation between the electron-trapping energy and on-site electrostatic potential energy of each site (Figure 5). There are only two notable exceptions: site 9 at the (001) surface and site 12 at the (111) surface. Trapping of electrons at both of these sites is more favorable than one would expect based on the electrostatic potential energy. The breakdown of the correlation for these sites could suggest that other effects are also influencing electron trapping at these sites, such as the strain energy required to distort the geometry of the system.[48] It is notable that these two sites are coordinated to only four oxygen
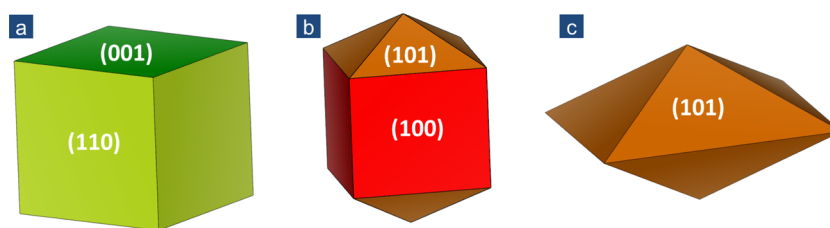
Figure 6. Nonequilibrium nanocrystal morphologies predicted to expose surfaces that (a) trap electrons strongly, (b) repel electrons, and (c) are weakly repulsive to electrons. The colors of the facets reflect their propensity to trap electrons (red representing strongly repulsive, light green representing weakly attractive, and orange representing weakly repulsive). Figures were produced using the VESTA 3D visualization program.[57]

atoms unlike any of the other sites considered and have the largest compressive strain in the relaxed surface (see Table 1). This reduced coordination would appear to be an important factor in stabilizing electron trapping. The electrostatic potential energies also help explain why we were unable to localize an electron at site 9 of the (110) surface. The electrostatic potential energy at this site is very high and is reflected in the local density of states which shows a dramatic shift of the d states to higher energies when compared to a bulk-like site (see Supporting Information). The electrostatic potential is also higher on sites 10 and 12 in the (111) surface slab but not prohibitively high. This suggests other factors may be preventing localization at this site, such as a high degree of orbital hybridization between neighboring sites.

Designing Optimal Nanocrystal Morphologies. The equilibrium crystal shape shown in Figure 2 involves a mixture of (110), (101), and (100) facets. The results detailed above show that the prevalent (110) facets contain surface and subsurface sites which are favorable for electron trapping. On the other hand, the (101) and (100) facets are both repulsive to electrons. The colors of the facets shown in Figure 2 reflect their propensity to trap electrons (red representing strongly repulsive, light green representing weakly attractive, and orange representing weakly repulsive). Therefore, on an equilibrium nanocrystal only about 50% of the total surface area is predicted to be able to trap electrons. For photocatalytic applications this is suboptimal as one would prefer electron trapping at all surfaces to maximize the surface area available to perform oxidation/reduction reactions. Indeed there is experimental evidence for face-dependent activities in anatase TiO_2 which lends general support to this idea.[51] The equilibrium shape is also not optimal for DSSC applications for a similar reason: about 50% of the surface area can trap electrons which will reduce electron mobility and may give rise to undesirable reactions with the electrolyte.[2,52−54]

With atomistic insight into the electron-trapping properties of all low index rutile TiO_2 surfaces we can design nanocrystal morphologies that exhibit properties that may be more desirable for applications. Synthesis of a wide range of nonequilibrium TiO_2 nanocrystal and nanowire morphologies is possible, for example, by altering the concentration of HCl during the synthesis or by using capping agents which selectively bind to surfaces to restrict the growth of certain facets,[55,56] making this a viable approach. For example, for photocatalytic applications nanocrystals should expose a higher proportion of electron-trapping surfaces. This can be achieved by forming cuboid or nanowire-type morphologies that expose only (001) and (110) surfaces (Figure 6a). Alternatively, nanocrystals with surfaces that have a low affinity to trap electrons can be formed by exposing only (100) and (101) surfaces (Figure 6b). For DSSC applications it is likely neither

of these options is optimal since if surfaces are highly repulsive to electrons the rate of intercrystal electron transfer may be reduced. A third option is a nanocrystal that exposes only weakly repulsive (101) surfaces such as the octahedral morphology shown in Figure 6c.

■ DISCUSSION AND CONCLUSIONS

We now discuss some of the factors which may affect the accuracy of the predictions made in this work. Depending on the site on which the electron is trapped the particular choice of the Hubbard U parameter may leave some residual SI error uncorrected affecting predictions of relative stability. We note that this issue is not specific to the DFT+U approach but applies in general to other SI-corrected methods such as hybrid functionals. Another potential issue is the presence of artificial image interactions introduced by the finite size of the supercell.[58] We note that a scheme has recently been developed that can correct calculated total energies for charged defects at surfaces to remove the effect of such spurious electrostatic interactions.[59] Application of this approach to charged defects at a NaCl surface suggests that the absolute formation energy of charged defects is strongly affected by such corrections, but relative energies for different defect positions within a slab are less affected. Since in this study all electron-trapping energies are defined with respect to an electron trapped in a bulk-like site in the same surface slab we similarly expect such energy differences to be reliable. Additionally the large supercells employed and the extremely high dielectric constant of TiO_2 should help to minimize these effects. To verify this expectation we conducted a supercell size scaling study for a polaron trapped at the (100) surface (see Supporting Information) and find that for the sizes of supercells employed in this study trapping energies are converged to 0.1 eV. Importantly variations in trapping energies at different surfaces span 1 eV ranging from positive to negative, much larger than the magnitude of any finite size effect error. Therefore, while such issues may affect the quantitative accuracy of predicted trapping energies, the general trends, and importantly whether a given surface is predicted to have a high electron affinity or not, are expected to be more robust. This is supported by the overall good correlation between electron-trapping energies and electrostatic potential energy since the latter is not affected strongly by image interactions or the choice of U.

Here, we have considered ideal defect-free low-index surfaces of rutile TiO_2 in order to gain insight into electron trapping at nanocrystal surfaces. There are a number of additional factors which may also influence electron trapping in applications. For example, the presence of adsorbed species such as hydroxyls and point defects such as vacancies will also influence the trapping of electrons at nanocrystal surfaces.[36,60] In DSSC applications dye molecules are also present, and the porous

nanocrystalline TiO_2 layer is immersed in an electrolyte which is known to capture electrons and reduce device efficiency.[2] These additional effects are clearly important areas for further study. Extended defects such as nanocrystal interfaces and steps may also affect electron trapping. In recent work we have studied the effect of trapping at a (210) grain boundary in TiO_2, finding that it contains a mixture of both high and low electron affinity sites again connected to variations in on-site electrostatic potential.[36]

In summary, we have investigated the interaction of electrons with all low index surfaces of rutile TiO_2 using density functional theory. We find that electron trapping at the surface of nanocrystals is highly anisotropic, with some surface facets having a propensity to trap electrons but others being repulsive. The trends in trapping can be linked to variations in electrostatic potential and ion coordination near the surface, consistent with previous studies of a range of metal oxide materials including MgO, ZrO_2, HfO_2, and TiO_2.[36,47−50] The results provide atomistic insight into electron trapping in TiO_2 nanocrystals, an issue which has proved extremely challenging to probe directly experimentally. Practically, the results can be used to provide guidance for materials design. Equilibrium nanocrystal morphologies predicted on the basis of surface formation energies expose both electron-trapping and electron-repelling surface facets. However, for particular applications, such as photocatalysis or DSSCs it may be desirable to expose only surfaces with similar electron affinities. On the basis of our results we propose a number of nonequilibrium nanocrystal morphologies which have this property and may offer improved performance for a number of applications.

The main conclusion of this work is that different surface facets on TiO_2 nanocrystals exhibit markedly different electron-trapping properties and that knowledge of their properties opens the way to knowledge-led design of nanocrystal morphologies for improved performance in applications. Furthermore, electron-trapping energies are found to be highly correlated with on-site electrostatic potential and coordination, providing a predictive guide to the trapping properties of surfaces. While results are presented for rutile TiO_2 which is a material with important and diverse applications, the key conclusions are expected to apply more generally to similar materials, including metal oxides and nitrides. Furthermore, similar correlations between charge trapping energies, electrostatic potential, and coordination should be expected for holes and excitons. Similar approaches to those described here could be employed to optimize the morphology of nanomaterials for wide ranging applications in solid-state lighting, solar cells, and photocatalysis.

■ ASSOCIATED CONTENT

Ⓢ Supporting Information

Convergence of surface formation energies, structural analysis of bulk-like Ti sites in the (100) surface slab, local density of states at Ti sites in the (110) surface slab, and finite size effects in calculation of trapping energies. This material is available free of charge via the Internet at http://pubs.acs.org.

■ AUTHOR INFORMATION

Corresponding Author

*E-mail: keith.mckenna@york.ac.uk.

Notes

The authors declare no competing financial interest.

■ REFERENCES

(1) O'Regan, B.; Grätzel, M. A low-cost, high-efficiency solar cell based on dye-sensitized colloidal TiO_2 films. *Nature* **1991**, *353*, 737−740.

(2) Peter, L. M. The Grätzel Cell: Where Next? *J. Phys. Chem. Lett.* **2011**, *2*, 1861−1867.

(3) Ni, M.; Leung, M. K. H.; Leung, D. Y. C.; Sumathy, K. A review and recent developments in photocatalytic water-splitting using TiO_2 for hydrogen production. *Renew. Sust. Energy Rev.* **2007**, *11*, 401−425.

(4) Linsebigler, A. L.; Lu, G.; Yates, J. T. Photocatalysis on TiO_2 Surfaces: Principles, Mechanisms, and Selected Results. *Chem. Rev.* **1995**, *95*, 735−758.

(5) Cedillo-González, E. I.; Riccó, R.; Montorsi, M.; Montorsi, M.; Falcaro, P.; Siligardi, C. Self-cleaning glass prepared from a commercial TiO_2 nano-dispersion and its photocatalytic performance under common anthropogenic and atmospheric factors. *Build. Environ.* **2014**, *71*, 7−14.

(6) Yu, J.; Sushko, M. L.; Kerisit, S.; Rosso, K. M.; Liu, J. Kinetic Monte Carlo Study of Ambipolar Lithium Ion and Electron-Polaron Diffusion into Nanostructured TiO_2. *J. Phys. Chem. Lett.* **2012**, *3*, 2076−2081.

(7) Deskins, N. A.; Dupuis, M. Electron transport via polaron hopping in bulk TiO_2: A density functional theory characterization. *Phys. Rev. B* **2007**, *75*, 195212.

(8) Deák, P.; Aradi, B.; Frauenheim, T. Quantitative theory of the oxygen vacancy and carrier self-trapping in bulk TiO_2. *Phys. Rev. B* **2012**, *86*, 195206.

(9) Janotti, A.; Franchini, C.; Varley, J. B.; Kresse, G.; Van de Walle, C. G. Dual behavior of excess electrons in rutile TiO_2. *Phys. Status Solidi - Rapid Res. Lett.* **2013**, *7*, 199−203.

(10) Sezen, H.; Buchholz, M.; Nefedov, A.; Natzeck, C.; Heissler, S.; Di, C.; Wöll, C. Probing electrons in TiO_2 polaronic trap states by IR-absorption: Evidence for the existence of hydrogenic states. *Sci. Rep.* **2014**, *4*, 1−4.

(11) Coronado, J. M.; Maira, A. J.; Conesa, J. C.; Yeung, K. L.; Augugliaro, V.; Soria, J. EPR Study of the Surface Characteristics of Nanostructured TiO_2 under UV Irradiation. *Langmuir* **2001**, *17*, 5368−5374.

(12) Kumar, C. P.; Gopal, N. O.; Wang, T. C.; Wong, M.-S.; Ke, S. C. EPR Investigation of TiO_2 Nanoparticles with Temperature-Dependent Properties. *J. Phys. Chem. B* **2006**, *110*, 5223−5229.

(13) Yang, S.; Brant, A. T.; Giles, N. C.; Halliburton, L. E. Intrinsic small polarons in rutile TiO_2. *Phys. Rev. B* **2013**, *87*, 125201.

(14) Chiesa, M.; Paganini, M. C.; Livraghi, S.; Giamello, E. Charge trapping in TiO_2 polymorphs as seen by Electron Paramagnetic Resonance spectroscopy. *Phys. Chem. Chem. Phys.* **2013**, *15*, 9435−9447.

(15) Setvin, M.; Franchini, C.; Hao, X.; Schmid, M.; Janotti, A.; Kaltak, M.; Van de Walle, C. G.; Kresse, G.; Diebold, U. Direct View at Excess Electrons in TiO_2 Rutile and Anatase. *Phys. Rev. Lett.* **2014**, *113*, 086402.

(16) Deskins, N. A.; Rousseau, R.; Dupuis, M. Localized Electronic States from Surface Hydroxyls and Polarons in TiO_2(110). *J. Phys. Chem. C* **2009**, *113*, 14583−14586.

(17) Kowalski, P. M.; Camellone, M. F.; Nair, N. N.; Meyer, B.; Marx, D. Charge Localization Dynamics Induced by Oxygen Vacancies on the TiO_2(110) Surface. *Phys. Rev. Lett.* **2010**, *105*, 146405.

(18) Ramamoorthy, M.; Vanderbilt, D. First-principles calculations of the energetics of stoichiometric TiO_2 surfaces. *Phys. Rev. B* **1994**, *49*, 16721−16727.

(19) Lee, S.-Y.; Park, S.-J. TiO$_2$ photocatalyst for water treatment applications. *J. Ind. Eng. Chem.* **2013**, *19*, 1761−1769.

(20) O'Regan, B.; Grätzel, M. A low-cost, high-efficiency solar cell based on dye-sensitized colloidal TiO$_2$ films. *Nature* **1991**, *353*, 737−40.

(21) Morgan, B. J.; Watson, G. W. A DFT+U description of oxygen vacancies at the TiO$_2$ rutile (110) surface. *Surf. Sci.* **2007**, *601*, 5034−5041.

(22) Scanlon, D. O.; Walsh, A.; Morgan, B. J.; Nolan, M.; Fearon, J.; Watson, G. W. Surface sensitivity in lithium-doping of MgO: A density functional theory study with correction for on-site Coulomb interations. *J. Phys. Chem. C* **2007**, *111*, 7971−7979.

(23) Nolan, M.; Parker, S. C.; Watson, G. W. The electronic structure of oxygen vacancy defects at the low index surfaces of ceria. *Surf. Sci.* **2005**, *595*, 223−232.

(24) Valentin, C. D.; Pacchioni, G.; Selloni, A. Electronic Structure of Defect States in Hydroxylated and Reduced Rutile TiO$_2$(110) Surfaces. *Phys. Rev. Lett.* **2006**, *97*, 166803.

(25) Calzado, C. J.; Hernández, N. C.; Sanz, J. F. Effect of on-site Coulomb repulsion term on the band-gap states of the reduced rutile (110) TiO$_2$ surface. *Phys. Rev. B* **2008**, *77*, 045118.

(26) Himmetoglu, B.; Floris, A.; de Gironcoli, S.; Cococcioni, M. Hubbard-corrected DFT energy functionals: The LDA+U description of correlated systems. *Int. J. Quantum Chem.* **2013**, *1151738*, 1−36.

(27) Spreafico, C.; VandeVondele, J. The nature of excess electrons in anatase and rutile from hybrid DFT and RPA. *Phys. Chem. Chem. Phys.* **2014**, *16*, 26144−52.

(28) Finazzi, E.; Di Valentin, C.; Pacchioni, G.; Selloni, A. Excess electron states in reduced bulk anatase TiO$_2$: comparison of standard GGA, GGA+U, and hybrid DFT calculations. *J. Chem. Phys.* **2008**, *129*, 154113.

(29) Calzado, C.; Hernández, N.; Sanz, J. Effect of on-site Coulomb repulsion term U on the band-gap states of the reduced rutile (110) TiO$_2$ surface. *Phys. Rev. B* **2008**, *77*, 045118.

(30) Morgan, B. J.; Watson, G. W. Polaronic trapping of electrons and holes by native defects in anatase TiO$_2$. *Phys. Rev. B* **2009**, *80*, 233102.

(31) Deskins, N. A.; Rousseau, R.; Dupuis, M. Distribution of Ti 3+ Surface Sites in Reduced TiO$_2$. *J. Phys. Chem. C* **2011**, *115*, 7562−7572.

(32) Yamamoto, T.; Ohno, T. A hybrid density functional study on the electron and hole trap states in anatase titanium dioxide. *Phys. Chem. Chem. Phys.* **2012**, *14*, 589−598.

(33) Lee, H.-Y.; Clark, S. J.; Robertson, J. Calculation of point defects in rutile TiO$_2$ by the screened-exchange hybrid functional. *Phys. Rev. B* **2012**, *86*, 075209.

(34) Morgan, B. J.; Scanlon, D. O.; Watson, G. W. Small polarons in Nb- and Ta-doped rutile and anatase TiO$_2$. *J. Mater. Chem.* **2009**, *19*, 5175−5178.

(35) Di Valentin, C.; Selloni, A. Bulk and Surface Polarons in Photoexcited Anatase TiO$_2$. *J. Phys. Chem. Lett.* **2011**, *2*, 2223−2228.

(36) Wallace, S. K.; McKenna, K. P. Grain Boundary Controlled Electron Mobility in Polycrystalline Titanium Dioxide. *Adv. Mater. Inter.* **2014**, *1*, 1400078.

(37) Morgan, B. J.; Watson, G. W. A DFT+U description of oxygen vacancies at the TiO$_2$ rutile (110) surface. *Surf. Sci.* **2007**, *601*, 5034−5041.

(38) Kresse, G.; FurthmAüller, J. Efficiency of ab-initio total energy calculations for metals and semiconductors using a plane-wave basis set. *Comput. Mater. Sci.* **1996**, *6*, 15−50.

(39) Kresse, G.; Furthmüller, J. Efficient iterative schemes for ab initio total-energy calculations using a plane-wave basis set. *Phys. Rev. B* **1996**, *54*, 11169−11186.

(40) Dudarev, S. L.; Botton, G. A.; Savrasov, S. Y.; Humphreys, C. J.; Sutton, A. P. Electron-energy-loss spectra and the structural stability of nickel oxide. *Phys. Rev. B* **1998**, *57*, 1505−1509.

(41) Morgan, B. J.; Watson, G. W. A DFT+U description of oxygen vacancies at the TiO$_2$ rutile (110) surface. *Surf. Sci.* **2007**, *601*, 5034−5041.

(42) Watson, G. W.; Kelsey, E. T.; de Leeuw, N. H.; Harris, D. J.; Parker, S. C. Atomistic simulation of dislocations, surfaces and interfaces in MgO. *J. Chem. Soc., Faraday Trans.* **1996**, *92*, 433.

(43) Wulff, G. Zur Frage der Geschwindigkeit des Wachstums und der Auflösung der Krystallflächen. *Z. Kristallogr. Miner.* **1901**, *34*, 449.

(44) Nazeeruddin, M. K.; Kay, A.; Rodicio; Humpbry-Baker, R.; Miller, E.; P. Liska, N. V.; Gratzel, M. Conversion of Light to Electricity by cis-XzBis (2,2′-bipyridyl-4,4′-dicarboxylate) ruthenium(11) Charge-Transfer Sensitizers (X = C1-, Br-, I-, CN-, and SCN-) on Nanocrystalline TiO$_2$ Electrodes. *J. Am. Chem. Soc.* **1993**, *115*, 6382−6390.

(45) Nakade, S.; Saito, Y.; Kubo, W.; Kitamura, T.; Wada, Y.; Yanagida, S. Influence of TiO$_2$ Nanoparticle Size on Electron Diffusion and Recombination in Dye-Sensitized TiO$_2$ Solar Cells. *J. Phys. Chem. B* **2003**, *107*, 8607−8611.

(46) Grätzel, M. Conversion of sunlight to electric power by nanocrystalline dye-sensitized solar cells. *J. Photochem. Photobiol., A: Chem.* **2004**, *164*, 3−14.

(47) McKenna, K. P.; Shluger, A. First-principles calculations of defects near a grain boundary in MgO. *Phys. Rev. B* **2009**, *79*, 224116.

(48) McKenna, K. P.; Wolf, M. J.; Shluger, A. L.; Lany, S.; Zunger, A. Two-Dimensional Polaronic Behavior in the Binary Oxides m-HfO$_2$ and m-ZrO$_2$. *Phys. Rev. Lett.* **2012**, *108*, 116403.

(49) Wolf, M. J.; McKenna, K. P.; Shluger, A. L. Hole Trapping at Surfaces of m-ZrO$_2$ and m-HfO$_2$ Nanocrystals. *J. Phys. Chem. C* **2012**, *116*, 25888.

(50) McKenna, K. P. Electronic and Chemical Properties of a Surface-Terminated Screw Dislocation in MgO. *J. Am. Chem. Soc.* **2013**, *135*, 18859−18865.

(51) Tachikawa, T.; Yamashita, S.; Majima, T. Evidence for Crystal-Face-Dependent TiO$_2$ Photocatalysis from Single-Molecule Imaging and Kinetic Analysis. *J. Am. Chem. Soc.* **2011**, *133*, 7197−7204.

(52) Cao, F.; Oskam, G.; Meyer, G. J.; Searson, P. C. Electron Transport in Porous Nanocrystalline TiO$_2$ Photoelectrochemical Cells. *J. Phys. Chem.* **1996**, *100*, 17021−17027.

(53) Hagfeldt, A.; Grätzel, M. Molecular Photovoltaics. *Acc. Chem. Res.* **2000**, *33*, 269−277.

(54) Benkstein, K. Influence of the percolation network geometry on electron transport in dye-sensitized titanium dioxide solar cells. *J. Phys. Chem. B* **2003**, *107*, 7759−7767.

(55) Dinh, C.-T.; Nguyen, T.-D.; Kleitz, F.; Do, T.-O. Shape-Controlled Synthesis of Highly Crystalline Titania Nanocrystals. *ACS Nano* **2009**, *3*, 3737−3743.

(56) Oh, J.-K.; Lee, J.-K.; Kim, S. J.; Park, K.-W. Synthesis of phase- and shape-controlled TiO$_2$ nanoparticles via hydrothermal process. *J. Ind. Eng. Chem.* **2009**, *15*, 270−274.

(57) Momma, K.; Izumi, F. VESTA 3 for three-dimensional visualization of crystal, volumetric and morphology data. *J. Appl. Crystallogr.* **2011**, *44*, 1272−1276.

(58) Lany, S.; Zunger, A. Assessment of correction methods for the band-gap problem and for finite-size effects in supercell defect calculations: Case studies for ZnO and GaAs. *Phys. Rev. B* **2008**, *78*, 235104.

(59) Komsa, H.-P.; Pasquarello, A. Finite-Size Supercell Correction for Charged Defects at Surfaces and Interfaces. *Phys. Rev. Lett.* **2013**, *110*, 095505.

(60) Gong, X.-Q.; Selloni, A.; Batzill, M.; Diebold, U. Steps on anatase TiO$_2$(101). *Nat. Mater.* **2006**, *5*, 665−70.